

Quasibound states of a charged Dirac field around regular black holes

Shao-Jun Zhang¹

Institute for Theoretical Physics and Cosmology, Zhejiang University of Technology, Hangzhou 310032, China

School of Physics and Optical Engineering, Zhejiang University of Technology, Hangzhou 310032, China

June 30, 2026

Abstract

We study quasibound states of a massive charged Dirac field on the Ayón-Beato–García (ABG) regular black-hole background and determine how a charged regular geometry modifies the fermionic spectrum in the absence of superradiant amplification. We derive the separated Dirac equations, impose quasibound boundary conditions, and obtain the far-field trapping condition $M\mu^2 - qQ\omega_R > 0$, whose weak-binding, same-sign limit is $M\mu > qQ$. The complex frequencies are computed in the frequency domain and checked against time-domain evolutions. Because ABG and Reissner–Nordström (RN) black holes have the same Newtonian and Coulomb tails, they share the leading hydrogenic real-frequency spectrum. Their differences appear in subleading shifts and, more prominently, in the damping rates. The ABG inner barrier can reduce the horizon flux, making some modes much longer lived than their RN counterparts. Within the explored parameter range, the Dirac quasibound modes remain damped: the regular charged geometry changes the lifetime of the fermionic cloud but does not produce a Dirac superradiant instability.

¹sjzhang@zjut.edu.cn

1 Introduction

Gravitational-wave detections and horizon-scale images now allow strong-field gravity to be tested through spectra, damping times, and near-horizon propagation [1–3]. Massive fields provide a complementary probe. A field whose Compton wavelength is comparable to the gravitational radius can be trapped outside a black hole by the mass barrier, forming quasibound states that slowly leak through the horizon. Their complex frequencies, $\omega = \omega_R + i\omega_I$ with $\omega_I < 0$, carry two pieces of information: ω_R is mainly fixed by the long-range gravitational and electromagnetic tails, while ω_I measures how efficiently the cloud is absorbed by the black hole [4–6]. Such long-lived states are relevant to black-hole spectroscopy, ultralight or effectively massive fields, and dynamical versions of black-hole “hair” [7–10].

Regular black holes provide a complementary setting for studying these spectra. The curvature singularity of classical black-hole solutions is widely viewed as a sign that the classical theory is being pushed beyond its domain of validity. One way to model possible short-distance corrections is to replace the singular core by a regular interior while keeping an event horizon and the same asymptotic charges. This idea goes back to Bardeen’s nonsingular black-hole model and Dymnikova’s vacuum nonsingular solution [11, 12]. It has since been realized in several effective settings, including nonlinear electrodynamics and higher-curvature or other effective constructions [13–21]. The altered inner geometry can affect both wave propagation and absorption. For example, quasinormal-mode studies of regular black holes show that the real parts can remain close to the Reissner–Nordström (RN) values while the damping rates are more sensitive to the regular-core structure [22].

The charged case makes this sensitivity particularly clear. RN black holes set the standard baseline for charged superradiance: charged scalar waves can extract electromagnetic energy from a charged horizon, but for a massive charged scalar field on an asymptotically flat RN black hole the superradiant condition and the mass-generated bound-state condition cannot be satisfied at the same time. The usual charged-scalar superradiant instability is therefore absent [23–25]. RN black holes can nevertheless become unstable when confinement is supplied by a mirror, a cavity, or a cosmological horizon [26–30]. Charged regular black holes are different. In the Ayón-Beato–García (ABG) geometry and related regular spacetimes, the nonlinear-electrodynamic structure modifies the electrostatic and trapping potentials; it can support charged scalar clouds, superradiant amplification, and superradiant instabilities in suitable parameter regions [31–35]. This contrast leads to the question addressed here: if the bosonic field is replaced by a fermionic one, does the regular charged geometry still leave a measurable imprint on the long-lived spectrum, or is the effect mainly a consequence of scalar superradiance?

Dirac fields are a good test of this question because their black-hole dynamics is not a copy of the scalar case. The propagation of spin-1/2 fields in curved spacetime has been studied since the early work on neutrinos in gravitational fields [36, 37]. A single-particle Dirac field does not undergo black-hole superradiant amplification [38, 39], and normalizable time-periodic Dirac clouds are excluded in standard black-hole backgrounds [40, 41]. Still, massive Dirac fields have well-defined scattering resonances, quasinormal modes, and quasibound states. These have been studied in Schwarzschild, RN, and Kerr geometries [42–48]. Dirac perturbations have also been used to probe regular and nonlinear-electrodynamic black holes, mostly through quasinormal modes and time-domain evolution [49, 50]. Charged massive Dirac quasibound states on a charged regular background have received less attention. A direct frequency- and time-domain comparison with RN at the same asymptotic mass and charge can isolate the effect of the regular geometry.

The ABG black hole provides a natural setting for this comparison. It is a regular charged solution of Einstein gravity coupled to nonlinear electrodynamics [13, 14]. At large radius its metric and electromagnetic potential approach those of RN, so the leading Newtonian and Coulomb terms should give the same weak-binding real spectrum. Differences between ABG and RN must therefore come from

subleading terms in the potential and from the near-horizon barrier that controls the leakage of the Dirac cloud into the black hole.

In this work we derive the separated massive charged Dirac equation on the ABG background and compute its quasibound spectrum. The large-radius analysis gives the general far-field trapping condition

$$M\mu^2 - qQ\omega_R > 0,$$

whose same-sign, near-threshold limit is $M\mu > qQ$. We solve the frequency-domain eigenvalue problem by two-sided shooting and matching, compare ABG and RN roots at the same dimensionless parameters, and use characteristic time evolution with matrix-pencil mode extraction as an independent dynamical check.

The paper is organized as follows. Section 2 introduces the ABG geometry and gauge convention. Section 3 derives the separated Dirac system, the asymptotic boundary conditions, and the leading existence criterion. Section 4 presents the frequency-domain method and the ABG–RN comparison. Section 5 describes the time-domain evolution and mode extraction. Section 6 summarizes the results and discusses their physical implications. We use natural units $G = c = \hbar = 4\pi\epsilon_0 = 1$, where G is Newton’s constant, c is the speed of light, \hbar is the reduced Planck constant, and ϵ_0 is the vacuum permittivity. The Fourier convention is $e^{-i\omega t}$ throughout.

2 ABG Black Holes

We consider the electrically charged Ayón-Beato–García (ABG) black-hole solution of nonlinear electrodynamics coupled to Einstein gravity [13, 14]. In static spherical coordinates, the line element is

$$ds^2 = -f(r)dt^2 + \frac{dr^2}{f(r)} + r^2(d\theta^2 + \sin^2\theta d\phi^2), \quad (1)$$

with the metric function

$$f(r) = 1 - \frac{2Mr^2}{(r^2 + Q^2)^{3/2}} + \frac{Q^2r^2}{(r^2 + Q^2)^2}. \quad (2)$$

Here M is the mass parameter and $Q > 0$ denotes the magnitude of the black-hole charge; the sign of the electromagnetic interaction is controlled by the field charge through the product qQ . For later convenience we define

$$\Delta(r) \equiv r^2 f(r). \quad (3)$$

The event-horizon radius r_h is the largest positive root of $f(r_h) = 0$. Near the center $r = 0$ one finds

$$f(r) = 1 + \left(\frac{1}{Q^2} - \frac{2M}{Q^3} \right) r^2 + \mathcal{O}(r^4), \quad (4)$$

or, equivalently, $f(r) = 1 - \Lambda_{\text{eff}} r^2/3 + \mathcal{O}(r^4)$ with $\Lambda_{\text{eff}} = 3(2M/Q^3 - 1/Q^2)$. On the black-hole branch considered here, where $Q < 2M$, this is the local static-patch expansion of a de Sitter-like core. For $Q > 2M$, the same local expansion would instead be anti-de Sitter-like. In either case, the polynomial curvature invariants remain finite at $r = 0$, so the geometry is regular in the curvature sense. At large radius,

$$f(r) = 1 - \frac{2M}{r} + \frac{Q^2}{r^2} + \mathcal{O}(r^{-3}), \quad (5)$$

so the geometry is asymptotically RN-like.

The ABG solution is supported by a nonlinear electromagnetic field. For the electric branch used

here, the potential has the radial electrostatic form $A_\mu = (A_t(r), 0, 0, 0)$, where

$$A_t(r) = -\frac{r^5}{2Q} \left(\frac{3M}{r^5} + \frac{2Q^2}{(Q^2 + r^2)^3} - \frac{3M}{(Q^2 + r^2)^{5/2}} \right). \quad (6)$$

Here we have adopted the gauge $A_t(\infty) = 0$. With this convention the frequency ω is the one measured by static observers at infinity. A constant gauge shift $A_t \rightarrow A_t + C$ is accompanied by $\omega \rightarrow \omega - qC$, leaving the combination $\omega + qA_t$ and hence the radial equations unchanged. The horizon quantity $\omega_c \equiv -qA_t(r_h)$ used below is therefore tied to this gauge choice; physical statements depend only on the corresponding potential difference between the horizon and infinity. Its large- r behavior is

$$A_t(r) = -\frac{Q}{r} - \frac{15MQ}{4r^2} + O(r^{-3}), \quad (7)$$

which matches the RN asymptotics at leading order, with subleading corrections that depend on the ABG parameters. This Coulomb tail controls the far-field trapping and decay conditions for charged quasibound states.

3 Equation of Motion and Asymptotics

3.1 Equation of Motion and Separation of Variables

We consider a massive charged Dirac field minimally coupled to the curved background and to the electromagnetic potential. Its equation of motion is

$$(\gamma^\mu D_\mu - \mu)\Psi = 0, \quad D_\mu = \partial_\mu - \Gamma_\mu - iqA_\mu. \quad (8)$$

Here minimal coupling means that gravity enters through the tetrad and spin connection, while the electromagnetic field enters only through the replacement $\partial_\mu \rightarrow \partial_\mu - iqA_\mu$; no Pauli-type or curvature-dependent nonminimal couplings are included. The field Ψ is a four-component spinor, μ and q are its mass and charge, γ^μ are the curved-space gamma matrices, and Γ_μ is the spin connection matrix. The curved gamma matrices are related to the flat ones $\hat{\gamma}^a$ by tetrads as

$$\gamma^\mu = e_a^\mu \hat{\gamma}^a, \quad \{\hat{\gamma}^a, \hat{\gamma}^b\} = 2\eta^{ab} I_4, \quad \{\gamma^\mu, \gamma^\nu\} = 2g^{\mu\nu} I_4. \quad (9)$$

Here I_4 is the 4×4 identity matrix. We choose the diagonal coframe

$$e^a{}_\mu = \text{diag} \left(\sqrt{f(r)}, \frac{1}{\sqrt{f(r)}}, r, r \sin \theta \right), \quad (10)$$

with inverse tetrad $e_a{}^\mu$, so that $g_{\mu\nu} e_a{}^\mu e_b{}^\nu = \eta_{ab}$ and $\eta_{ab} = \text{diag}(-1, 1, 1, 1)$. Frame indices are raised and lowered with η_{ab} , while coordinate indices are raised and lowered with the spacetime metric $g_{\mu\nu}$. The spin connection matrices are computed from the tetrad through

$$\Gamma_\mu = -\frac{1}{4} \omega_{\mu ab} \hat{\gamma}^a \hat{\gamma}^b, \quad \omega_{\mu ab} = e_{a\nu} \nabla_\mu e_b{}^\nu. \quad (11)$$

We use a Weyl/chiral representation of the flat gamma matrices [44],

$$\begin{aligned}\hat{\gamma}^0 &= i \begin{pmatrix} O & I_2 \\ I_2 & O \end{pmatrix}, & \hat{\gamma}^1 &= i \begin{pmatrix} O & \sigma_3 \\ -\sigma_3 & O \end{pmatrix}, \\ \hat{\gamma}^2 &= i \begin{pmatrix} O & \sigma_1 \\ -\sigma_1 & O \end{pmatrix}, & \hat{\gamma}^3 &= i \begin{pmatrix} O & \sigma_2 \\ -\sigma_2 & O \end{pmatrix},\end{aligned}\tag{12}$$

where I_2 is the 2×2 identity matrix, O is the 2×2 zero matrix, and σ_i are the Pauli matrices

$$\sigma_1 = \begin{pmatrix} 0 & 1 \\ 1 & 0 \end{pmatrix}, \quad \sigma_2 = \begin{pmatrix} 0 & -i \\ i & 0 \end{pmatrix}, \quad \sigma_3 = \begin{pmatrix} 1 & 0 \\ 0 & -1 \end{pmatrix}.\tag{13}$$

Because the background is static and spherically symmetric, the field can be decomposed as [44, 45]

$$\Psi = \frac{1}{\sqrt{r} \Delta^{1/2}} \begin{pmatrix} \psi_-(r, \theta) \\ \psi_+(r, \theta) \end{pmatrix} e^{-i\omega t} e^{im\phi},\tag{14}$$

where

$$\psi_- = - \begin{pmatrix} R_2(r) S_1(\theta) \\ R_1(r) S_2(\theta) \end{pmatrix}, \quad \psi_+ = \begin{pmatrix} R_1(r) S_1(\theta) \\ R_2(r) S_2(\theta) \end{pmatrix}.\tag{15}$$

Here R_1 and R_2 are radial functions, S_1 and S_2 are angular functions, and m is the azimuthal quantum number. The frequency ω is measured in the gauge $A_t(\infty) = 0$. The prefactor in (14) gives the standard first-order form of the separated equations. The pairing of radial and angular functions ensures that the two sets of operators close separately on (R_1, R_2) and (S_1, S_2) .

Substituting (14) into the Dirac equation (8), using (9)–(10), yields a coupled system for $R_1, R_2, S_1,$ and S_2 . Introducing

$$\mathcal{D}_\pm \equiv \sqrt{\Delta} \left(\frac{d}{dr} \pm \frac{iK}{\Delta} \right), \quad \mathcal{L}_\pm \equiv \frac{d}{d\theta} + \frac{1}{2} \cot \theta \pm m \csc \theta,\tag{16}$$

the four component equations can be written as

$$\mathcal{D}_- R_1 S_1 + \mathcal{L}_+ S_2 R_2 - i\mu r R_2 S_1 = 0,\tag{17}$$

$$\mathcal{D}_+ R_2 S_2 - \mathcal{L}_- S_1 R_1 + i\mu r R_1 S_2 = 0,\tag{18}$$

$$\mathcal{D}_+ R_2 S_1 + \mathcal{L}_+ S_2 R_1 + i\mu r R_1 S_1 = 0,\tag{19}$$

$$\mathcal{D}_- R_1 S_2 - \mathcal{L}_- S_1 R_2 - i\mu r R_2 S_2 = 0.\tag{20}$$

The angular dependence in these four relations enters through $\mathcal{L}_- S_1$ and $\mathcal{L}_+ S_2$. Separation gives the two-component angular eigenvalue problem

$$\left(\frac{d}{d\theta} + \frac{1}{2} \cot \theta - m \csc \theta \right) S_1 = +\lambda S_2\tag{21}$$

$$\left(\frac{d}{d\theta} + \frac{1}{2} \cot \theta + m \csc \theta \right) S_2 = -\lambda S_1\tag{22}$$

for modes of definite total angular momentum, with λ as the separation constant. Once (21)–(22) are

imposed, the radial equations reduce to

$$\sqrt{\Delta} \left(\frac{d}{dr} - \frac{iK}{\Delta} \right) R_1 = (\lambda + i\mu r) R_2, \quad (23)$$

$$\sqrt{\Delta} \left(\frac{d}{dr} + \frac{iK}{\Delta} \right) R_2 = (\lambda - i\mu r) R_1, \quad (24)$$

where

$$K(r) = r^2 [\omega + qA_t(r)]. \quad (25)$$

The combination $\omega + qA_t$ is the gauge-covariant frequency, and $K(r)$ packages it in the radial equations. Equations (23) and (24) are related by $i \rightarrow -i$ and $R_1 \leftrightarrow R_2$. The angular eigenvalue condition is [51]

$$|\lambda| = j + \frac{1}{2}, \quad j = \frac{1}{2}, \frac{3}{2}, \dots \quad (26)$$

The corresponding angular solutions are the usual spin-1/2 spherical harmonics. For each half-integer j and each $m = -j, -j+1, \dots, j$, the pair (S_1, S_2) has two branches, corresponding to $\lambda = \pm \left(j + \frac{1}{2} \right)$, and is determined, up to overall normalization, by regularity at $\theta = 0, \pi$. For spectral labeling it is useful to introduce the orbital angular number ℓ , which distinguishes these two spinor branches at fixed j :

$$\lambda_{j\ell} = \begin{cases} +\ell = + \left(j + \frac{1}{2} \right), & \ell = j + \frac{1}{2}, \\ -1 - \ell = - \left(j + \frac{1}{2} \right), & \ell = j - \frac{1}{2}. \end{cases} \quad (27)$$

Thus λ is fixed by regularity of the angular spinor harmonics on the sphere and then enters the radial equations as the separation constant. The azimuthal number m controls the angular dependence within a given multiplet, whereas the radial spectrum is determined by the boundary-value problem (23)–(24) at fixed $\lambda_{j\ell}$. In what follows, individual frequency families may therefore be labeled by the more physical set (n_r, j, ℓ) , where n_r denotes the radial excitation number within a fixed angular branch, while the radial equations are written in terms of λ .

3.2 Second-Order Form and Effective Potential

The coupled first-order radial equations (23)–(24) can be decoupled into second-order equations for R_1 and R_2 :

$$\sqrt{\Delta} \frac{d}{dr} \left(\sqrt{\Delta} \frac{dR_1}{dr} \right) - \frac{i\mu\Delta}{\lambda + i\mu r} \frac{dR_1}{dr} + U_1(r) R_1 = 0, \quad (28)$$

$$\sqrt{\Delta} \frac{d}{dr} \left(\sqrt{\Delta} \frac{dR_2}{dr} \right) + \frac{i\mu\Delta}{\lambda - i\mu r} \frac{dR_2}{dr} + U_2(r) R_2 = 0, \quad (29)$$

where $U_1(r)$ is given by

$$U_1(r) = \frac{1}{\Delta} \left(K^2 + \frac{1}{2} iK \frac{d\Delta}{dr} \right) - i \frac{dK}{dr} - \frac{\mu K}{\lambda + i\mu r} - (\lambda^2 + \mu^2 r^2), \quad (30)$$

and $U_2 = U_1(i \rightarrow -i)$.

The equation (28) for R_1 can be transformed into a Schrödinger-like form by introducing the tortoise

coordinate

$$\frac{dx}{dr} = \frac{1}{f(r)} = \frac{r^2}{\Delta(r)}, \quad (31)$$

together with the scaling $\psi_1 = F^{-1}R_1$ with

$$F(r) = \frac{\Delta^{1/4}}{r} \left(1 + \frac{i\mu r}{\lambda}\right)^{1/2}. \quad (32)$$

This gives

$$\frac{d^2\psi_1}{dx^2} - V_1(r)\psi_1 = 0, \quad (33)$$

with the effective potential

$$V_1(r) = -\frac{\Delta}{r^4}U_1 - \frac{1}{8r^4} \left(\frac{d\Delta}{dr}\right)^2 + \frac{\Delta}{2r^5} \frac{d\Delta}{dr} - \frac{\Delta^2}{r^4 F} \frac{d^2 F}{dr^2} + \frac{\Delta^2}{2r^5} \frac{\mu(\mu r - 2i\lambda)}{(\lambda + i\mu r)^2}. \quad (34)$$

With the sign convention in (33), $V_1(r)$ plays the role of an effective potential for a zero-energy Schrödinger problem. The corresponding equation for R_2 follows by the replacement $i \rightarrow -i$, together with $\psi_1 \leftrightarrow \psi_2$, so that $V_2 = V_1(i \rightarrow -i)$.

3.3 Boundary Conditions for Quasibound States

Near the event horizon $r = r_h$, the effective potentials $V_{1,2}(r)$ behave as

$$V_{1,2}(r) \approx -\left(\omega - \omega_c \pm \frac{i}{4}f'(r_h)\right)^2 + \mathcal{O}(r - r_h), \quad r \rightarrow r_h, \quad (35)$$

where $\omega_c \equiv -qA_t(r_h)$ is the critical frequency defined by the electromagnetic potential at the horizon; the sign is + for V_1 and – for V_2 . The leading behavior of the radial functions is controlled by the indicial equation, which gives ingoing and outgoing branches. The ingoing branch is

$$\begin{pmatrix} R_1 \\ R_2 \end{pmatrix} \sim \begin{pmatrix} e^{f'(r_h)x/4} \\ e^{-f'(r_h)x/4} \end{pmatrix} (r - r_h)^{1/4} e^{-i(\omega - \omega_c)x} \sim \begin{pmatrix} (r - r_h)^{1/2} \\ 1 \end{pmatrix} (r - r_h)^{\rho_h}, \quad r \rightarrow r_h, \quad (36)$$

where

$$\rho_h = -\frac{i(\omega - \omega_c)}{f'(r_h)}. \quad (37)$$

At spatial infinity, the effective potentials $V_{1,2}(r)$ behave as

$$V_{1,2}(r) = (\mu^2 - \omega^2) + \frac{2(qQ\omega - M\mu^2)}{r} + \mathcal{O}(r^{-2}), \quad r \rightarrow \infty. \quad (38)$$

These asymptotic expansions are identical to those of the RN case, as expected because the ABG geometry and gauge field approach the RN solution at large radius. The same far-field analysis therefore applies, and the leading behavior of the radial functions at infinity is

$$R_{1,2} \sim r^\chi e^{kr}, \quad r \rightarrow \infty, \quad (39)$$

with

$$k = -\sqrt{\mu^2 - \omega^2}, \quad \chi = \frac{M(\mu^2 - 2\omega^2) + qQ\omega}{k}. \quad (40)$$

Quasibound states require $\text{Re}(k) < 0$, which selects the solution that decays at infinity. For the weakly damped, positive-frequency modes considered below, this condition implies

$$\omega_R < \mu, \quad (41)$$

so the real part of the mode frequency lies below the mass threshold.

3.4 Leading Existence Inequality

For the leading real-potential argument, we replace ω in (38) by ω_R . Then

$$\frac{dV_{1,2}}{dr} = \frac{2(M\mu^2 - qQ\omega_R)}{r^2} + O(r^{-3}). \quad (42)$$

Since the wave equation has the form $\psi'' - V\psi = 0$, the bound-state tail is exponentially decaying when $V \rightarrow \mu^2 - \omega^2 > 0$ at infinity. To form an outer trapping region, the leading $1/r$ correction must lower the effective potential as one moves inward from infinity, so that an oscillatory region can develop at finite radius. This gives the necessary far-field condition

$$M\mu^2 - qQ\omega_R > 0. \quad (43)$$

This condition is independent of the sign of qQ . For repulsive electromagnetic coupling, $qQ > 0$, it constrains the competition between gravity and electric repulsion and can be written as

$$\omega_R < \frac{M\mu^2}{qQ}. \quad (44)$$

For attractive electromagnetic coupling, $qQ < 0$, the electromagnetic interaction acts in the same direction as gravity and the condition is correspondingly easier to satisfy. This does not prevent quasibound states from forming: the mass term gives an exponentially decaying tail at infinity, the attractive long-range force localizes the field at finite radius, and the ingoing horizon condition makes the state quasibound rather than strictly bound. In the near-threshold regime relevant for weakly bound massive modes, $\omega \simeq \mu$, (43) becomes

$$M\mu - qQ > 0. \quad (45)$$

For $qQ > 0$, this gives the nontrivial same-sign condition $M\mu > qQ$; for $qQ < 0$, it is automatically satisfied because the electromagnetic force is attractive. Away from the near-threshold limit, however, the relevant far-field condition is still the frequency-dependent inequality (43). This leading argument is only a *necessary* criterion for an outer trapping tendency; the actual existence of a discrete quasibound spectrum still depends on the full radial potential and the ingoing boundary condition at the horizon.

3.5 Hydrogenic Approximation

The hydrogenic estimate is a weak-coupling far-zone result. We take

$$O(|qQ|) = O(M\mu) \equiv O(\epsilon), \quad \epsilon \ll 1. \quad (46)$$

The levels are then shallow, $\omega_R - \mu = O(\mu\epsilon^2)$, and the wave function is supported mainly at radii much larger than the black-hole scale. Using (38) in the Schrödinger-like equation for either component ψ_a

($a = 1, 2$), and using $x \simeq r$ at large radius, gives

$$\frac{d^2\psi_a}{dr^2} + \left[\omega_R^2 - \mu^2 + \frac{2(M\mu^2 - qQ\omega_R)}{r} + \mathcal{O}(r^{-2}) \right] \psi_a = 0. \quad (47)$$

Since $\omega_R = \mu + \mathcal{O}(\mu\epsilon^2)$, the Coulomb coupling is

$$\alpha_{\text{eff}} = M\mu - qQ. \quad (48)$$

Thus $\alpha_{\text{eff}} > 0$ is the weak-binding limit of (43). Keeping only the threshold and Coulomb terms, the ABG and RN backgrounds are indistinguishable: both have the same leading Newtonian term and the same leading electrostatic potential. The real part of the spectrum therefore has the universal hydrogenic form [45, 52]

$$1 - \frac{\omega_R}{\mu} \simeq \frac{(M\mu - qQ)^2}{2N^2} + \mathcal{O}(\epsilon^4), \quad (49)$$

or equivalently

$$\omega_R \simeq \mu \left[1 - \frac{(M\mu - qQ)^2}{2N^2} \right]. \quad (50)$$

Here

$$N = n_r + \ell + 1, \quad n_r = 0, 1, 2, \dots, \quad (51)$$

with n_r the radial excitation number at fixed (j, ℓ) . Using (27),

$$N = \begin{cases} n_r + j + \frac{1}{2}, & \ell = j - \frac{1}{2} \quad (\lambda < 0), \\ n_r + j + \frac{3}{2}, & \ell = j + \frac{1}{2} \quad (\lambda > 0). \end{cases} \quad (52)$$

Thus the two signs of λ start from different principal levels at fixed j . If $N = n + j + 1/2$ is used as a single spectral label, then $n = n_r$ on the $\lambda < 0$ branch and $n = n_r + 1$ on the $\lambda > 0$ branch.

The leading formula (49) does not depend on the regular core. The first analytic ABG–RN separation appears when the next far-zone term is retained. Denoting by $\beta_a^{(X)}$ the coefficient of the $1/r^2$ correction to the Coulomb radial problem, the expansion gives, for both spinor components,

$$\beta_a^{(\text{ABG})} = \beta_a^{(\text{RN})} + \frac{15}{2} MqQ\omega_R + \mathcal{O}(\epsilon^3). \quad (53)$$

The calculation leading to (53) is given in Appendix A. The resulting leading ABG–RN shift of the real frequency is

$$\omega_{R,a}^{\text{ABG}} - \omega_{R,a}^{\text{RN}} \simeq \frac{15}{4} \frac{MqQ\mu\omega_R\alpha_{\text{eff}}^2}{N^3\left(\ell + \frac{1}{2}\right)} = \frac{15}{4} \frac{MqQ\mu^2\alpha_{\text{eff}}^2}{N^3\left(\ell + \frac{1}{2}\right)} + \mathcal{O}(\mu\epsilon^5). \quad (54)$$

Thus the leading Coulomb spectrum is RN-like, while the first explicit ABG–RN difference is a fine-structure effect. The sign of the far-zone shift follows the sign of qQ within the weak-coupling expansion; the numerical spectrum also contains near-horizon matching effects that are not captured by this estimate.

4 Frequency-Domain Analysis

4.1 Frequency-Domain Method

For fixed dimensionless parameters $(Q/M, M\mu, qM)$ and angular labels (j, ℓ) , we choose $\lambda = \lambda_{j\ell}$ from (27) and solve the first-order radial system (23)–(24) as a complex eigenvalue problem,

$$\omega_{n_r j \ell} = \omega_R + i\omega_I. \quad (55)$$

The two branches $\ell = j \pm 1/2$ enter through different values of $\lambda_{j\ell}$ and therefore define different radial eigenvalue problems. The leading hydrogenic degeneracy is organized by $N = n_r + \ell + 1$, so comparisons between branches are made at fixed N .

The boundary conditions are ingoing behavior at the event horizon and exponential decay at spatial infinity. We impose them by two-sided shooting. The first-order system is integrated directly; the decoupled second-order equations are used only to diagnose the asymptotic behavior. Continued fractions provide a useful RN benchmark [45, 46, 53], but the non-rational ABG functions do not lead to the same simple recurrence relations, so shooting is used as the main method.

Near the horizon we start from the ingoing Frobenius branch in (36). Since the horizon itself is a singular endpoint of the radial coordinate, the outward integration is initialized at $r_0 = r_h + \epsilon_h$, where $\epsilon_h > 0$ is a small near-horizon cutoff:

$$\begin{pmatrix} R_1 \\ R_2 \end{pmatrix}_{r_0} = C_h (r_0 - r_h)^{\rho_h} \begin{pmatrix} (r_0 - r_h)^{1/2} \sum_{n=0}^{N_h} a_n^{(h)} (r_0 - r_h)^n \\ \sum_{n=0}^{N_h} c_n^{(h)} (r_0 - r_h)^n \end{pmatrix} \quad (56)$$

where ρ_h is given in (37). We fix the arbitrary local scale by setting $c_0^{(h)} = 1$; the remaining coefficients are obtained recursively from (23)–(24). The series is truncated at order N_h .

At spatial infinity the physical solution must approach the decaying branch in (39). In the numerical problem this condition is imposed at a finite outer cutoff r_∞ , chosen sufficiently large that the asymptotic expansion is valid. For a trial ω satisfying $\text{Re } k < 0$, the far-field spinor is seeded as

$$\begin{pmatrix} R_1 \\ R_2 \end{pmatrix}_{r_\infty} = C_\infty r_\infty^\chi e^{kr_\infty} \begin{pmatrix} \sum_{n=0}^{N_\infty} a_n^{(\infty)} r_\infty^{-n} \\ \sum_{n=0}^{N_\infty} b_n^{(\infty)} r_\infty^{-n} \end{pmatrix} \quad (57)$$

with k and χ defined in (40). We set $a_0^{(\infty)} = 1$ and determine the remaining inverse-power coefficients in the same way. The finite choices of r_∞ and N_∞ are varied as part of the convergence test. The arbitrary normalizations C_h and C_∞ are set to unity, since they do not affect the matching condition.

For a given trial frequency, the horizon solution is integrated outward and the far-field solution inward to a matching radius r_m . At an eigenfrequency the two solutions must be linearly dependent at r_m . This gives the scalar condition

$$\mathcal{D}(\omega) = \det \begin{pmatrix} R_1^{\text{hor}}(r_m) & R_1^\infty(r_m) \\ R_2^{\text{hor}}(r_m) & R_2^\infty(r_m) \end{pmatrix} = 0. \quad (58)$$

The zero of the determinant is invariant under independent rescalings of the two local solutions.

Numerically, (58) is solved as two real equations for (ω_R, ω_I) , with initial guesses inside the quasibound window

$$0 < \omega_R < \mu, \quad \omega_I < 0, \quad (59)$$

guided by the hydrogenic estimate (49). Once a root is found, parameter continuation in μ , q , or Q is used to follow the same branch.

We accept a root only if it satisfies $\text{Re } k < 0$, has an isolated residual minimum, and remains stable when $r_m, \epsilon_h, r_\infty, N_h, N_\infty$, and the ODE tolerances are varied. The digits quoted in the tables are the digits that survive these checks, with particular attention to ω_I . As a calibration, the same code is applied to RN and reproduces continued-fraction benchmark roots within the displayed accuracy.

4.2 Numerical Results

We report $M\omega_R$ and $-M\omega_I$, with $-\omega_I > 0$ the damping rate. Modes are labeled by (n_r, j, ℓ) and by the separation constant $\lambda_{j\ell}$ in (27). For every ABG root, we compute the corresponding RN root at the same $(Q/M, M\mu, qM, n_r, j, \ell)$. This point-by-point comparison separates the effect of the geometry from changes caused by the field parameters or mode labels.

The large-radius analysis predicts that the ABG and RN real frequencies should be close because the two backgrounds have the same leading Newtonian and Coulomb tails and hence the same leading hydrogenic spectrum (49). Their damping rates can differ more substantially because they depend on the wave transmitted through the inner potential and absorbed by the horizon. Table 1 gives a reference spectrum at $M\mu = 0.4$, $qQ = 0.1$, and $Q/M = 0.5$ and identifies the mode families followed below. The radial number n_r is counted separately within each (j, ℓ) branch, and the leading hydrogenic principal number is $N = n_r + \ell + 1$.

Table 1: Reference frequency-domain quasibound spectrum for $M = 1$, $Q/M = 0.5$, $M\mu = 0.4$, and $qM = 0.2$, for which $qQ = 0.1$ and $M\mu - qQ = 0.3$. Here n_r is the radial excitation number of each (j, ℓ) branch, so the leading hydrogenic principal number is $N = n_r + \ell + 1$. The RN frequencies are included for comparison, and $\Delta_R = M(\omega_R^{\text{ABG}} - \omega_R^{\text{RN}})$ and $\mathcal{R}_I = |\omega_I^{\text{ABG}}|/|\omega_I^{\text{RN}}|$; thus $\mathcal{R}_I < 1$ means that the ABG mode decays more slowly than the corresponding RN mode.

N	n_r	j	ℓ	$\lambda_{j\ell}$	$M\omega^{\text{ABG}}$	$M\omega^{\text{RN}}$	Δ_R	\mathcal{R}_I
1	0	1/2	0	-1	0.381793 - 0.003940i	0.380507 - 0.014634i	0.001286	0.269
2	1	1/2	0	-1	0.394912 - 0.000873i	0.394686 - 0.002358i	0.000226	0.370
	0	1/2	1	+1	0.395000 - 0.000045i	0.394084 - 0.000416i	0.000916	0.109
	0	3/2	1	-2	0.395505 - $1.58 \times 10^{-7}i$	0.394936 - $5.40 \times 10^{-6}i$	0.000569	0.029
3	1	1/2	1	+1	0.397785 - 0.000019i	0.397518 - 0.000146i	0.000267	0.128

At the reference point, the ABG real parts are all slightly larger than the RN values, but the shifts are small compared with the frequencies themselves. This is consistent with (54): the leading hydrogenic term is common to both backgrounds, and the first explicit ABG–RN correction is suppressed in the weak-binding expansion. The damping rates show a much clearer difference. The ratios \mathcal{R}_I range from 0.029 to 0.370, which corresponds to ABG lifetimes from a few times to more than an order of magnitude longer than the matched RN lifetimes. In this example, horizon leakage is therefore a more sensitive probe of the inner geometry than the position of the real-frequency level.

The leading hydrogenic degeneracy is also lifted. The three $N = 2$ modes have different complex frequencies because the exact radial problem depends on $\lambda_{j\ell}$ and not only on N . The RN spectrum already contains such a splitting; the ABG geometry adds a small real-frequency shift and a larger change in the leakage rate. Figure 1 shows the wider branch structure by following several ABG modes as $M\mu$ is

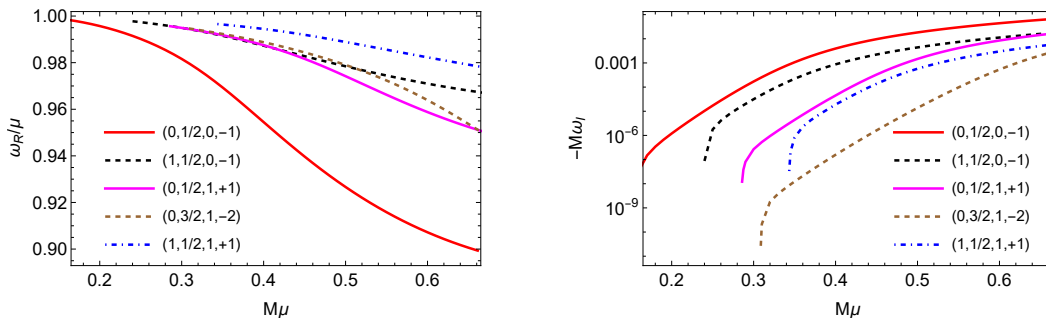


Figure 1: Dependence of the ABG quasibound frequencies on the mass coupling $M\mu$ for several (n_r, j, ℓ, λ) branches at fixed $Q/M = 0.5$ and $qM = 0.2$. The left panel shows ω_R/μ , while the right panel shows the damping rate $-M\omega_I$ on a logarithmic scale.

varied.

The real parts of the different branches remain close to the mass threshold, but their damping rates can differ by several orders of magnitude. In particular, modes with the same leading value of N are separated once the full radial equations and the matching to the horizon are taken into account. Near weak binding, some roots lie very close to the real axis and become difficult to continue numerically. The endpoints shown in the figure mark the range over which a root was tracked reliably, rather than a physical termination of the branch.

To study the parameter dependence without mixing different mode families, we now follow the fundamental $(n_r, j, \ell, \lambda) = (0, 1/2, 0, -1)$ branch in both geometries. The first scan varies $M\mu$ at fixed $Q/M = 0.5$ and $qM = 0.2$, so qQ is fixed while the effective attraction $\alpha_{\text{eff}} = M\mu - qQ$ changes.

As seen in Fig. 2, ω_R/μ decreases as $M\mu$ grows, in agreement with the increase in hydrogenic binding. The ABG and RN curves remain close, and the small difference Δ_R changes sign within the computed interval. The real-frequency shift is thus not controlled by a single far-zone correction; the full radial matching contributes at the same subleading order. The damping rates separate more clearly. We find $\mathcal{R}_I < 1$ throughout this scan, with the largest relative suppression on the weak-binding side. There the cloud extends farther from the black hole, so a change in the inner transmission produces a large relative change in the small flux that reaches the horizon.

The second scan, shown in Fig. 3, varies qQ at fixed $Q/M = 0.5$ and $M\mu = 0.4$. It therefore tunes the Coulomb interaction directly: negative qQ strengthens the attraction, while positive qQ weakens it and moves the mode toward the threshold $\omega_R = \mu$.

The real frequency follows this Coulomb trend, but Δ_R is nonmonotonic, again showing that the weak-binding estimate and the inner matching cannot be separated in the full solution. The lifetime comparison also changes across the scan. For negative or weakly positive qQ , the ABG mode can decay faster than the RN mode; at larger positive qQ , \mathcal{R}_I falls well below unity. A regular center does not by itself guarantee a longer-lived mode. What matters is the transmission from the outer cloud through the potential between the cloud and the horizon.

The sharp decrease of $|\omega_I|$ at larger positive qQ follows from the weakening effective attraction. As α_{eff} approaches zero from above, the state becomes weakly bound, spreads to larger radius, and develops a smaller amplitude near the horizon. All branches displayed here remain in the $\alpha_{\text{eff}} > 0$ trapping regime. We do not continue them into the $M\mu < qQ$ region, where the late-time response is instead expected to be tail-dominated.

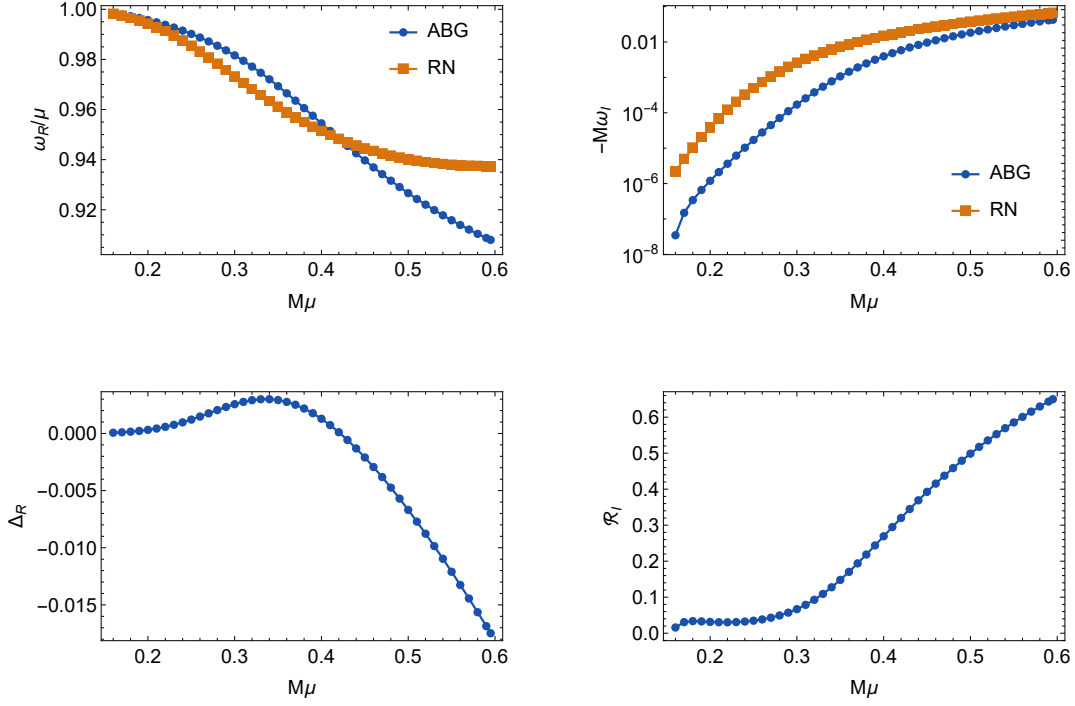


Figure 2: ABG–RN comparison for the dependence of the quasibound frequency on the mass coupling $M\mu$ for the fundamental $(n_r, j, \ell, \lambda) = (0, 1/2, 0, -1)$ branch at fixed $Q/M = 0.5$ and $qM = 0.2$. The real part is normalized by μ , and the lower panels show $\Delta_R = M(\omega_R^{\text{ABG}} - \omega_R^{\text{RN}})$ and $\mathcal{R}_I = |\omega_I^{\text{ABG}}|/|\omega_I^{\text{RN}}|$.

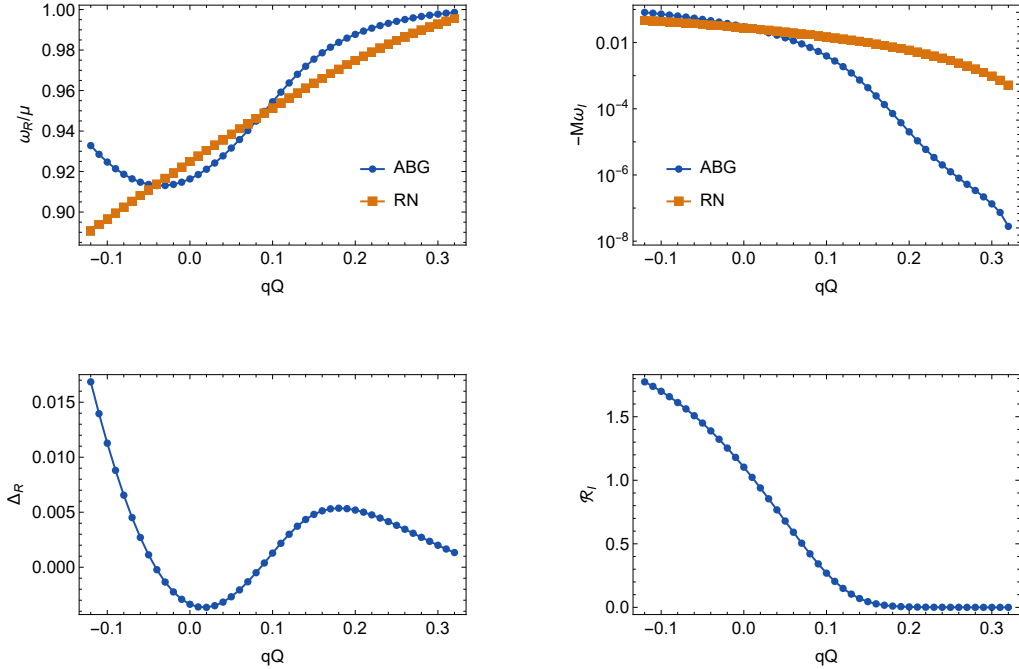


Figure 3: ABG–RN comparison for the dependence of the quasibound frequency on the electromagnetic coupling qQ for the fundamental $(n_r, j, \ell, \lambda) = (0, 1/2, 0, -1)$ branch at fixed $Q/M = 0.5$ and $M\mu = 0.4$. The upper panels show ω_R/μ and $-M\omega_I$, while the lower panels show $\Delta_R = M(\omega_R^{\text{ABG}} - \omega_R^{\text{RN}})$ and $\mathcal{R}_I = |\omega_I^{\text{ABG}}|/|\omega_I^{\text{RN}}|$.

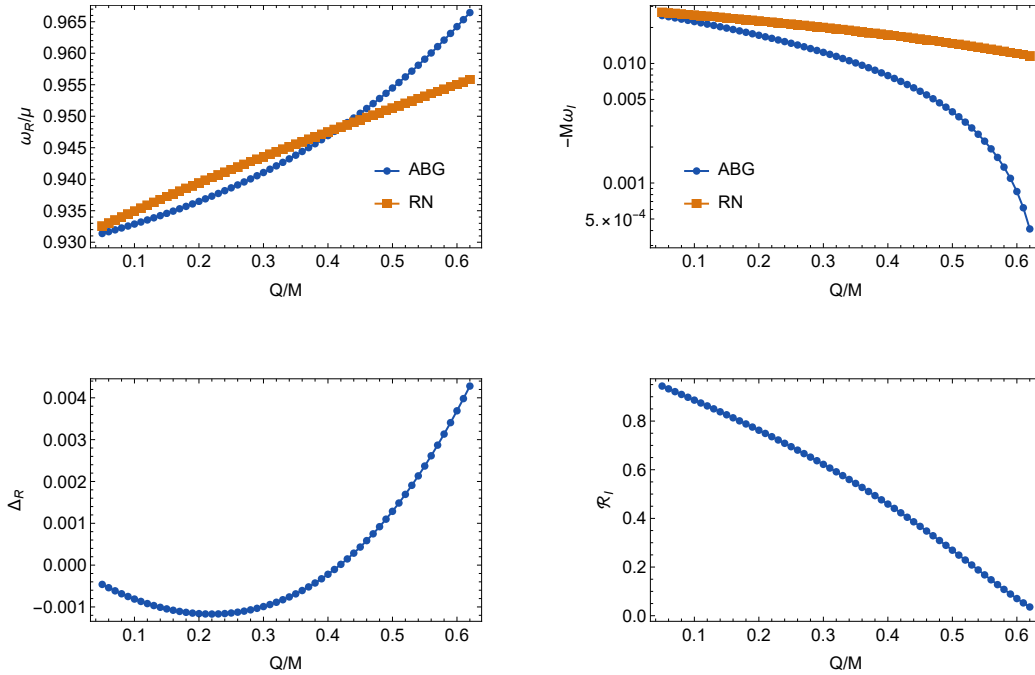


Figure 4: ABG–RN comparison for the dependence of the quasibound frequency on the black-hole charge Q/M for the fundamental $(n_r, j, \ell, \lambda) = (0, 1/2, 0, -1)$ branch at fixed $M\mu = 0.4$ and $qM = 0.2$. The upper panels show ω_R/μ and $-M\omega_I$, while the lower panels show $\Delta_R = M(\omega_R^{\text{ABG}} - \omega_R^{\text{RN}})$ and $\mathcal{R}_I = |\omega_I^{\text{ABG}}|/|\omega_I^{\text{RN}}|$.

The final scan varies Q/M at fixed $M\mu = 0.4$ and $qM = 0.2$. In this scan, changing the black-hole charge changes both the common Coulomb coupling qQ and the difference between the ABG and RN inner geometries.

The two spectra approach one another as $Q/M \rightarrow 0$, where both backgrounds reduce to Schwarzschild. As the charge increases, the real-frequency shift remains small because the leading outer potentials are still the same. The damping rate changes much more strongly, reflecting the growing difference between the two inner geometries. Although the slope of each curve contains both Coulomb and geometric effects, the ABG–RN comparison at any fixed value of Q/M is made with the same qQ and therefore isolates the difference between the two backgrounds.

The effective potential explains why the real and imaginary parts respond differently. Figure 5 compares $\text{Re } V_1$ for representative points from the $M\mu$, qQ , and Q/M scans.

With the sign convention of (33), a region with $\text{Re } V_1 > 0$ acts as a barrier in the corresponding zero-energy problem. The far-zone trapping region sets the binding scale and the spatial extent of the cloud. Because the leading ABG and RN potentials agree there, their ω_R values differ only slightly. The damping rate is controlled by the small fraction of the wave that crosses the inner barrier and enters the horizon. A change in the height or width of this barrier can therefore produce a large relative change in $|\omega_I|$ while leaving ω_R almost unchanged.

Comparing the solid and dashed curves at fixed parameters shows how the two backgrounds differ. Where the ABG modes are much longer lived, the ABG potential has a higher or more developed positive peak near the horizon. This is clearest for positive qQ and for larger Q/M . The additional barrier suppresses the flux entering the ABG horizon and accounts for $|\omega_I^{\text{ABG}}| < |\omega_I^{\text{RN}}|$. When the two inner potentials are close, as in the small- Q/M limit, their damping rates are also closer. At $qQ = -0.1$, by contrast, the ABG curve has no corresponding positive inner peak, and the ABG mode can decay faster

than the RN mode. The lifetime ordering is therefore set by the inner transmission, not by regularity alone.

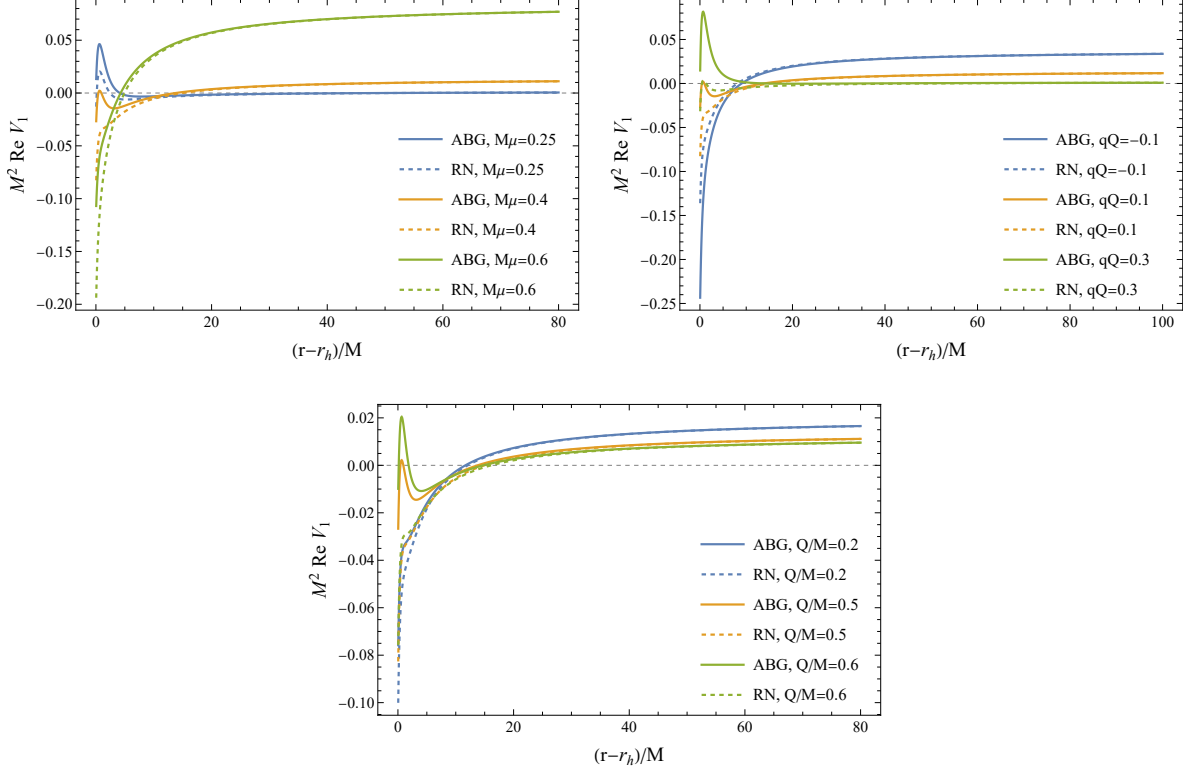


Figure 5: Effective-potential diagnostics for the fundamental $(n_r, j, \ell, \lambda) = (0, 1/2, 0, -1)$ branch. The quantity plotted is $M^2 \text{Re } V_1$ in the Schrödinger-like equation (33), evaluated at the leading hydrogenic real frequency ω_R^H in (49). Solid curves denote ABG, and dashed curves denote RN. The horizontal coordinate is shifted by the outer horizon of each background. The upper-left, upper-right, and lower panels use the same representative parameter choices as the scans in Figs. 2, 3, and 4, respectively. Since V_1 depends on the frequency, this figure is used as a qualitative diagnostic of the trapping and leakage structure, not as an independent eigenvalue calculation.

The solid ABG curves also account for the parameter dependence of the damping rate. In the upper-left panel, the positive near-horizon peak is lowered as $M\mu$ increases and is absent for the largest value displayed. The reduced barrier allows more flux to reach the horizon, consistent with the increase of $-M\omega_I$.

In the upper-right panel, increasing qQ raises the near-horizon potential. A high, narrow barrier is present at $qQ = 0.3$, whereas there is no positive peak at $qQ = -0.1$. The increasing barrier suppresses the horizon flux and explains the decrease of $-M\omega_I$.

In the Q/M panel, the ABG inner peak grows markedly between $Q/M = 0.2$ and 0.6 , leading to the strong decrease of the damping rate as the charge is increased. Since qQ also changes in this scan, this interpretation remains qualitative; the full variation of ω_I cannot be attributed to the barrier height alone.

5 Time-Domain Analysis

5.1 Evolution Equations and Numerical Method

The time-domain calculation independently checks the frequency-domain quasibound spectrum. Instead of imposing a complex-frequency ansatz, we evolve the radial Dirac system in the tortoise coordinate (31).

With $r = r(x)$ understood implicitly, the evolution equations are

$$\partial_t R_1 + \partial_x R_1 - iqA_t(r)R_1 = \sqrt{f(r)} \left(i\mu + \frac{\lambda}{r} \right) R_2, \quad (60)$$

$$\partial_t R_2 - \partial_x R_2 - iqA_t(r)R_2 = \sqrt{f(r)} \left(i\mu - \frac{\lambda}{r} \right) R_1. \quad (61)$$

This first-order form makes the characteristic structure explicit: R_1 and R_2 propagate in opposite radial directions and are coupled by the mass and spin-angular terms. For an observer at $x = x_{\text{obs}}$ and an evolution time T , only the part of the initial slice lying inside the past light cone, $x \in [x_{\text{obs}} - T, x_{\text{obs}} + T]$, can affect the recorded signal. We therefore evolve the system on this causal diamond rather than on a large rectangular domain. The two outer edges of the diamond are characteristics, so no artificial inner or outer boundary condition is imposed during the evolution.

Smooth localized initial data are used to excite the quasibound spectrum. We use generic wave-packet data, rather than imposing a frequency-domain eigenfunction as initial data, so that the time-domain calculation remains an independent dynamical test. A convenient choice is

$$R_1(0, x) = A \exp \left[-\frac{(x - x_g)^2}{2\sigma^2} \right], \quad R_2(0, x) = 0, \quad (62)$$

although the late-time frequencies are expected to be independent of this particular profile provided the initial data have nonzero overlap with the relevant modes. Changing x_g and σ only changes the relative excitation amplitudes of the modes and of the prompt response. On the causal grid we evolve Eqs. (60) and (61) with a second-order Crank–Nicolson scheme along the two characteristic directions, as in characteristic time-domain evolutions of black-hole perturbations [35, 45, 54]. We take the time step equal to the spatial step in the tortoise coordinate and check convergence by reducing this common grid spacing.

After the prompt response has passed, the signal at x_{obs} is described by a superposition of damped quasibound modes,

$$R_a(t, x_{\text{obs}}) \sim \sum_n A_{an} e^{-i\omega_n t}, \quad \omega_n = \omega_{R,n} + i\omega_{I,n}, \quad \omega_{I,n} < 0. \quad (63)$$

The complex frequencies are extracted by fitting the late-time complex signal to this damped exponential sum using the matrix-pencil method, a Prony-type mode-extraction technique [55–57]. We retain only frequencies that remain stable under changes of the fitting window, the number of fitted modes, and the grid spacing.

5.2 Numerical Results

The time-domain calculation provides a dynamical check of the frequency-domain roots. Since Sec. 4 already compares ABG and RN in the frequency domain, this section focuses on the ABG geometry. We use the same background parameters as in Table 1 and select the angular channel $(j, \ell, \lambda) = (1/2, 1, +1)$,

$$M = 1, \quad Q/M = 0.5, \quad M\mu = 0.4, \quad qM = 0.2, \quad \lambda = +1. \quad (64)$$

For this choice $qQ = 0.1$ and $M\mu - qQ = 0.3$. The modes are weakly damped enough to leave visible quasibound ringing, but their damping rates are still large enough to be probed within a finite time-domain evolution. The complementary same-sign regime $M\mu < qQ$ is not used as the benchmark case.

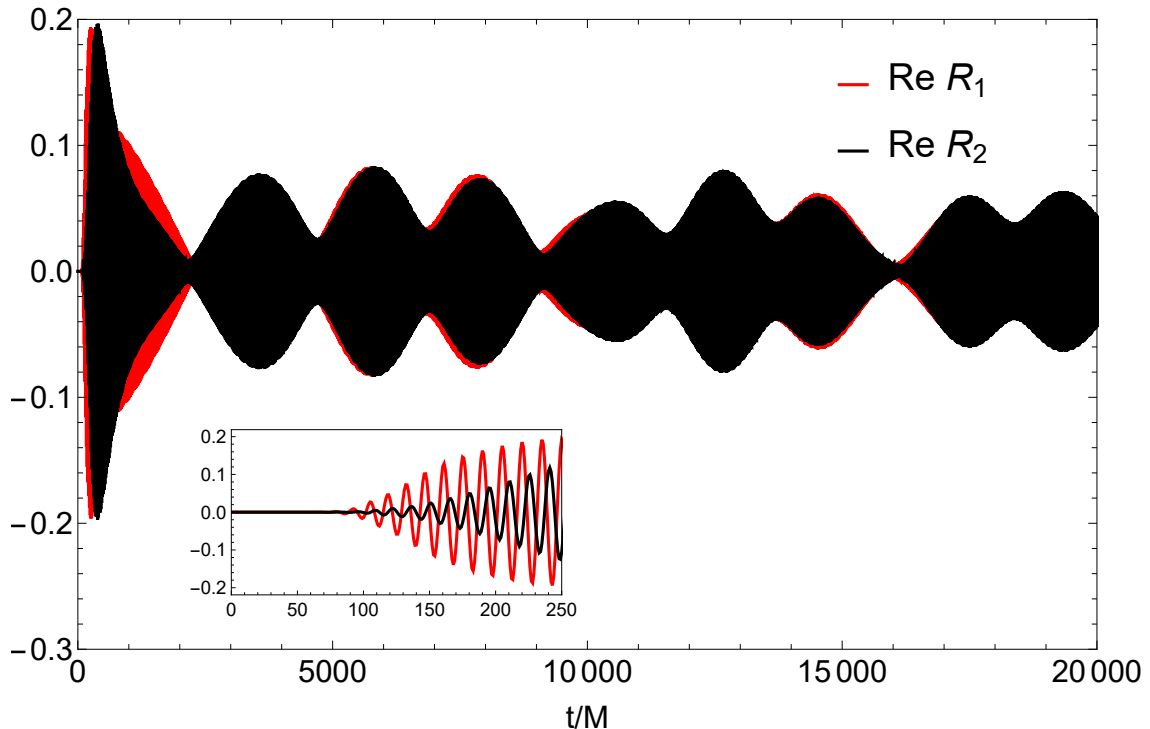


Figure 6: Representative ABG time-domain waveform for the benchmark point (64). The observer is placed at $x_{\text{obs}} = 80$, and the initial data are a Gaussian packet with $x_g = 7$ and $\sigma = 8$. The inset shows the early-time response, while the main panel displays the long-lived quasibound ringing and the beating pattern produced by nearby modes in $\text{Re } R_1$ and $\text{Re } R_2$.

In this complementary regime the far-field Coulomb interaction is effectively repulsive, so a long-lived hydrogenic quasibound branch is not expected to dominate the response. After the prompt response and possible quasinormal ringing have decayed, the asymptotically late signal should instead approach the massive Dirac tail $R_{1,2} \sim t^{-5/6} \sin(\mu t + \delta)$ found for charged massive Dirac fields on RN backgrounds [45, 58]. Since the ABG and RN geometries have the same leading far-field Coulomb structure, the same tail law is expected for ABG, with differences mainly in the transient amplitudes, phases, and crossover time.

Figure 6 shows the waveform recorded at $x_{\text{obs}} = 80$. The initial Gaussian packet is centered at $x_g = 7$ with width $\sigma = 8$, so it has appreciable overlap with the quasibound cloud while remaining separated from the observer at $t = 0$. The signal begins with a prompt response and then enters a slowly damped quasibound stage in which R_1 and R_2 oscillate with the same mode frequencies but different phases and amplitudes. The broad envelope modulation is a beating pattern caused by the superposition of nearby long-lived modes, as also occurs in time-domain studies of Dirac quasibound states [44, 45]. The frequencies extracted from this stage are listed in Table 2. For the parameters (64), the reference frequencies are obtained first by the same two-sided shooting method described in Sec. 4. The time-domain frequencies are then extracted from the complex waveform by a matrix-pencil fit to the late-time signal. Let Ω_{obs} denote the fitted oscillation frequency at x_{obs} , with $r_{\text{obs}} = r(x_{\text{obs}})$. To compare it with the frequency-domain (FD) value in the gauge $A_t(\infty) = 0$, we remove the local electromagnetic phase shift and define $\omega_{\text{TD}} = \Omega_{\text{obs}} - qA_t(r_{\text{obs}})$. The comparison is shown in Table 2. Increasing n_r pushes ω_R closer to the mass threshold μ and reduces the damping rate, so the higher radial excitations are longer lived but harder to isolate from a finite signal. The values quoted below are obtained from a long evolution with $t_{\text{max}} = 10^5 M$ and $\Delta x = \Delta t = 0.5M$; the fitting window is varied as a stability check.

The corrected real parts in Table 2 agree well with the shooting results at the same benchmark point.

Table 2: Comparison between frequency-domain and time-domain frequencies for the ABG benchmark point. Here ω_{FD} denotes the complex quasibound-state frequency obtained from the frequency-domain shooting method, whereas ω_{TD} denotes the frequency extracted from the late-time waveform by the matrix-pencil method. All entries use the parameters in (64) and $(j, \ell, \lambda) = (1/2, 1, +1)$. The time-domain values are corrected by $-qA_t(r_{\text{obs}})$ to the gauge $A_t(\infty) = 0$.

n_r	$M\omega_{\text{FD}}$	$M\omega_{\text{TD}}$
0	$0.395000 - 4.53 \times 10^{-5}i$	$0.395053 - 4.38 \times 10^{-5}i$
1	$0.397785 - 1.86 \times 10^{-5}i$	$0.397796 - 1.66 \times 10^{-5}i$
2	$0.398773 - 8.55 \times 10^{-6}i$	$0.398796 - 5.70 \times 10^{-6}i$
3	$0.399299 - 4.49 \times 10^{-6}i$	$0.399415 - 2.92 \times 10^{-6}i$

The damping rates of the first two modes are also reproduced with good accuracy. For the higher radial excitations the real parts remain stable, but the imaginary parts are more sensitive to the fitting window because the modes are long lived and overlap with nearby components of the signal; the $n_r = 3$ entry should therefore be read mainly as an identification of the corresponding long-lived component. The time-domain signal confirms the frequency-domain mode content, while the most precise damping rates are still taken from the shooting calculation.

6 Summary and Discussion

We studied quasibound modes of a massive charged Dirac field on the ABG regular black-hole background and compared them with the RN case. The radial Dirac equations form a coupled first-order system with ingoing behavior at the horizon and exponential decay at infinity. Their large-radius expansion gives

$$M\mu^2 - qQ\omega_R > 0, \quad (65)$$

as the leading trapping condition. The simpler inequality $M\mu > qQ$ follows only for same-sign charges in the weak-binding limit $\omega_R \simeq \mu$. It is not a general condition on the sign of qQ .

The frequency-domain calculation gives discrete damped Dirac quasibound modes within the parameter ranges explored here. No root with $\omega_I > 0$ was found. This numerical result is limited to the scanned parameter ranges, but it is consistent with the absence of black-hole superradiant amplification for the minimally coupled single-particle Dirac equation [38, 39]. It should not be extended to arbitrary fermionic effective theories. The result differs from the charged-scalar case, in which some regular charged black holes can be superradiantly unstable.

The ABG–RN comparison shows where the regular geometry matters. Since ABG and RN have the same leading Newtonian and Coulomb tails, their leading hydrogenic real-frequency spectrum is the same. Their real parts separate only through subleading terms and full radial matching. The damping rates are more sensitive to the inner geometry. The effective-potential comparison shows the mechanism: a higher or wider inner barrier reduces the flux that reaches the horizon, so the quasibound cloud decays more slowly. This explains why several ABG modes in the scans are longer lived than their RN counterparts, sometimes by more than one order of magnitude.

The time-domain calculation checks the same mode content without imposing a complex-frequency ansatz. Generic Gaussian initial data excite several nearby quasibound components, producing the beating pattern in Fig. 6. After correcting the local electromagnetic phase at the observation point, the matrix-pencil extraction reproduces the real parts of the frequency-domain roots well. The imaginary parts of the longest-lived overtones are harder to extract from a finite signal, because the modes decay

slowly and overlap with nearby components. The shooting calculation is therefore the more accurate source for damping rates, while the time-domain signal confirms that the same long-lived modes are dynamically excited.

The physical scale is set by the black-hole mass. Restoring International System of Units (SI) quantities requires the same charge normalization as in the RN/ABG metric. With $G = c = \hbar = 4\pi\epsilon_0 = 1$ [34],

$$M_{\text{geom}} = \frac{GM_{\text{BH}}}{c^2}, \quad Q_{\text{geom}} = \sqrt{\frac{G}{4\pi\epsilon_0 c^4}} Q_{\text{SI}}, \quad M\mu = \frac{GM_{\text{BH}}m_f}{\hbar c}, \quad qQ = \frac{q_{\text{SI}}Q_{\text{SI}}}{4\pi\epsilon_0\hbar c}.$$

Here M_{BH} is the physical black-hole mass, while m_f and q_{SI} are the mass and charge of the Dirac particle. The conversion of the frequency itself depends only on the dimensionless product $M\omega$,

$$M\omega = \frac{GM_{\text{BH}}}{c^3} \omega_{\text{phys}}.$$

Therefore

$$f_R = \frac{\omega_R^{\text{phys}}}{2\pi} \simeq 3.23 \times 10^4 \text{ Hz} \left(\frac{M_\odot}{M_{\text{BH}}} \right) (M\omega_R), \quad \tau = \frac{1}{|\omega_I^{\text{phys}}|} \simeq 4.93 \times 10^{-6} \text{ s} \left(\frac{M_{\text{BH}}}{M_\odot} \right) \frac{1}{|M\omega_I|}. \quad (66)$$

For the long-lived modes in Table 2, $M\omega_R \simeq 0.4$ and $|M\omega_I| \sim 10^{-6}$ – 10^{-5} . For a $10 M_\odot$ black hole this corresponds to an oscillation frequency of order 10^3 Hz and a damping time of seconds to tens of seconds. For a $10^6 M_\odot$ black hole the frequency is of order 10^{-2} Hz and the damping time is days to weeks. These lifetimes are long compared with the light-crossing time of the black hole. Direct observability is a separate question, because the present calculation treats a test Dirac field. The moderate charge ratios used in the numerical examples are therefore best viewed as theoretical probes that magnify the ABG–RN difference; in the small Q/M limit the two geometries approach the same Schwarzschild behavior and the regular-geometry corrections become correspondingly harder to resolve. A measurable signal would require a mechanism that excites a coherent fermionic configuration or couples the fermionic dynamics to an observable channel.

The present study is still limited in scope. The mode search covers selected branches rather than the full spectrum, and closely spaced roots require careful continuation and residual checks. Backreaction is neglected, and the ABG spacetime is treated as a fixed background. Further work could track the branches more densely in (q, μ, Q) and extend the analysis to rotating charged regular black holes, where electromagnetic coupling and frame dragging can compete.

Acknowledgments

This work is supported by the National Natural Science Foundation of China under Grant No. 12075207.

A Subleading Term in the Hydrogenic Expansion

This appendix gives the derivation of (53) and (54). For either spinor component, the next far-zone term in the Schrödinger-like potential can be written as

$$V_a^{(X)}(r) = \kappa^2 - \frac{2\mu\alpha_{\text{eff}}}{r} + \frac{\lambda(\lambda+1) + \beta_a^{(X)}}{r^2} + \mathcal{O}(r^{-3}), \quad \kappa^2 = \mu^2 - \omega_R^2, \quad X = \text{ABG, RN}. \quad (67)$$

The common RN part of β_a contains the spin-dependent and subleading RN geometry/electromagnetic terms. To isolate the ABG correction, write the far-zone electrostatic potential as

$$A_t^{(X)}(r) = -\frac{Q}{r} + \frac{a_2^{(X)}}{r^2} + \mathcal{O}(r^{-3}), \quad a_2^{(\text{RN})} = 0, \quad a_2^{(\text{ABG})} = -\frac{15MQ}{4}. \quad (68)$$

Then

$$K = r^2[\omega + qA_t(r)] = \omega r^2 - qQr + qa_2^{(X)} + \mathcal{O}(r^{-1}). \quad (69)$$

At order $1/r^2$ in the Schrödinger-like potential (34), the background-dependent contribution from $a_2^{(X)}$ comes only from the term $-K^2/r^4$. Indeed,

$$-\frac{K^2}{r^4} = -\omega^2 + \frac{2qQ\omega}{r} - \frac{(qQ)^2 + 2q\omega a_2^{(X)}}{r^2} + \mathcal{O}(r^{-3}). \quad (70)$$

The $a_2^{(X)}$ pieces in dK/dr and in $K/(\lambda + i\mu r)$ first enter at order r^{-3} . The ABG metric differs from the RN metric only at the next inverse power in the far-zone expansion, so it also does not change the $1/r^2$ coefficient. Therefore

$$\beta_a^{(\text{ABG})} - \beta_a^{(\text{RN})} = -2q\omega_R \left(a_2^{(\text{ABG})} - a_2^{(\text{RN})} \right) = \frac{15}{2}MqQ\omega_R, \quad (71)$$

independently of the spinor component $a = 1, 2$ at this order.

The $1/r^2$ term may then be treated as a perturbation of the Coulomb problem. For the unperturbed hydrogenic state,

$$\left\langle \frac{1}{r^2} \right\rangle_{N\ell} = \frac{\mu^2 \alpha_{\text{eff}}^2}{N^3 \left(\ell + \frac{1}{2} \right)}. \quad (72)$$

Thus

$$\omega_{R,a}^{(X)} = \mu \left[1 - \frac{\alpha_{\text{eff}}^2}{2N^2} \right] + \frac{\mu \alpha_{\text{eff}}^2 \beta_a^{(X)}}{2N^3 \left(\ell + \frac{1}{2} \right)} + \delta\omega_{\text{common}} + \dots, \quad (73)$$

where $\delta\omega_{\text{common}}$ denotes terms common to ABG and RN at the order retained. Substituting the ABG–RN difference in β_a gives (54).

References

- [1] B. P. Abbott *et al.*, “Observation of gravitational waves from a binary black hole merger,” *Phys. Rev. Lett.* **116** (2016) 061102, [arXiv:1602.03837](#).
- [2] K. Akiyama *et al.*, “First M87 event horizon telescope results. I. The shadow of the supermassive black hole,” *Astrophys. J. Lett.* **875** (2019) L1, [arXiv:1906.11238](#).
- [3] K. Akiyama *et al.*, “First Sagittarius A* event horizon telescope results. I. The shadow of the supermassive black hole in the center of the Milky Way,” *Astrophys. J. Lett.* **930** (2022) L12, [arXiv:2311.08680](#).
- [4] S. Detweiler, “Klein-Gordon equation and rotating black holes,” *Phys. Rev. D* **22** (1980) 2323.
- [5] S. R. Dolan, “Instability of the massive Klein-Gordon field on the Kerr spacetime,” *Phys. Rev. D* **76** (2007) 084001, [arXiv:0705.2880](#).

- [6] R. A. Konoplya and A. Zhidenko, “Quasinormal modes of black holes: From astrophysics to string theory,” *Rev. Mod. Phys.* **83** (2011) 793, [arXiv:1102.4014](#).
- [7] R. Brito, V. Cardoso, and P. Pani, *Superradiance: New Frontiers in Black Hole Physics*, vol. 906 of *Lecture Notes in Physics*. Springer, 2015. [arXiv:1501.06570](#).
- [8] A. Arvanitaki, S. Dimopoulos, S. Dubovsky, N. Kaloper, and J. March-Russell, “String axiverse,” *Phys. Rev. D* **81** (2010) 123530, [arXiv:0905.4720](#).
- [9] J. Barranco, A. Bernal, J. C. Degollado, A. Diez-Tejedor, M. Megevand, M. Alcubierre, D. Nunez, and O. Sarbach, “Are black holes a serious threat to scalar field dark matter models?” *Phys. Rev. D* **84** (2011) 083008, [arXiv:1108.0931](#).
- [10] J. Barranco, A. Bernal, J. C. Degollado, A. Diez-Tejedor, M. Megevand, M. Alcubierre, D. Nunez, and O. Sarbach, “Schwarzschild black holes can wear scalar wigs,” *Phys. Rev. Lett.* **109** (2012) 081102, [arXiv:1207.2153](#).
- [11] J. M. Bardeen, “Non-singular general-relativistic gravitational collapse,” in *Proceedings of the International Conference GR5*, p. 174. Tbilisi University Press, Tbilisi, U.S.S.R., 1968.
- [12] I. Dymnikova, “Vacuum nonsingular black hole,” *Gen. Relativ. Gravit.* **24** (1992) 235–242.
- [13] E. Ayón-Beato and A. García, “Regular black hole in general relativity coupled to nonlinear electrodynamics,” *Phys. Rev. Lett.* **80** (1998) 5056, [arXiv:gr-qc/9911046](#).
- [14] E. Ayón-Beato and A. García, “New regular black hole solution from nonlinear electrodynamics,” *Phys. Lett. B* **464** (1999) 25, [arXiv:hep-th/9911174](#).
- [15] E. Ayón-Beato and A. García, “The Bardeen model as a nonlinear magnetic monopole,” *Phys. Lett. B* **493** (2000) 149–152, [arXiv:gr-qc/0009077](#).
- [16] K. A. Bronnikov, “Regular magnetic black holes and monopoles from nonlinear electrodynamics,” *Phys. Rev. D* **63** (2001) 044005, [arXiv:gr-qc/0006014](#).
- [17] I. Dymnikova, “Regular electrically charged structures in nonlinear electrodynamics coupled to general relativity,” *Class. Quantum Grav.* **21** (2004) 4417–4429, [arXiv:gr-qc/0407072](#).
- [18] S. A. Hayward, “Formation and evaporation of regular black holes,” *Phys. Rev. Lett.* **96** (2006) 031103, [arXiv:gr-qc/0506126](#).
- [19] Z.-Y. Fan and X. Wang, “Construction of regular black holes in general relativity,” *Phys. Rev. D* **94** (2016) 124027, [arXiv:1610.02636](#).
- [20] C. Lan, H. Yang, Y. Guo, and Y.-G. Miao, “Regular black holes: a short topic review,” *Int. J. Theor. Phys.* **62** (2023) 202, [arXiv:2303.11696](#).
- [21] K. A. Bronnikov, “Regular black holes sourced by nonlinear electrodynamics,” 2022. [arXiv:2211.00743](#).
- [22] A. Flachi and J. P. S. Lemos, “Quasinormal modes of regular black holes,” *Phys. Rev. D* **87** (2013) 024034, [arXiv:1211.6212](#).
- [23] H. Furuhashi and Y. Nambu, “Instability of massive scalar fields in Kerr-Newman spacetime,” *Prog. Theor. Phys.* **112** (2004) 983, [arXiv:gr-qc/0402037](#).

- [24] S. Hod, “Stability of the extremal Reissner-Nordström black hole to charged scalar perturbations,” *Phys. Lett. B* **713** (2012) 505.
- [25] S. Hod, “No-bomb theorem for charged Reissner-Nordström black holes,” *Phys. Lett. B* **718** (2013) 1489–1492.
- [26] C. A. R. Herdeiro, J. C. Degollado, and H. F. Rúnarsson, “Rapid growth of superradiant instabilities for charged black holes in a cavity,” *Phys. Rev. D* **88** (2013) 063003, [arXiv:1305.5513](#).
- [27] S. R. Dolan, S. Ponglertsakul, and E. Winstanley, “Stability of black holes in einstein-charged scalar field theory in a cavity,” *Phys. Rev. D* **92** (2015) 124047, [arXiv:1507.02156](#).
- [28] O. J. C. Dias and R. Masachs, “Charged black hole bombs in a Minkowski cavity,” *Class. Quantum Grav.* **35** (2018) 184001, [arXiv:1801.10176](#).
- [29] Z. Zhu, S.-J. Zhang, C. E. Pellicer, B. Wang, and E. Abdalla, “Stability of Reissner–Nordström black hole in de Sitter background under charged scalar perturbation,” *Phys. Rev. D* **90** (2014) 044042, [arXiv:1405.4931](#). Addendum: *Phys. Rev. D* **90**, 049904 (2014).
- [30] R. A. Konoplya and A. Zhidenko, “Charged scalar field instability between the event and cosmological horizons,” *Phys. Rev. D* **90** (2014) 064048, [arXiv:1406.0019](#).
- [31] S. Hod, “Spatially regular charged black holes supporting charged massive scalar clouds,” *Phys. Rev. D* **109** (2024) 064074, [arXiv:2401.07907](#).
- [32] M. A. A. de Paula, L. C. S. Leite, S. R. Dolan, and L. C. B. Crispino, “Absorption and (unbounded) superradiance in a static regular black hole spacetime,” 2024. [arXiv:2401.01767](#).
- [33] S. R. Dolan, M. A. A. de Paula, and L. C. B. Crispino, “Superradiant instability of a charged regular black hole,” *Phys. Rev. D* **109** (2024) 124037, [arXiv:2401.14967](#).
- [34] Y. Zhan, H. Xu, and S.-J. Zhang, “Charged superradiant instability in a spherical regular black hole,” *Eur. Phys. J. C* **84** (2024) 1315, [arXiv:2410.19261](#).
- [35] Y. Zhan, H. Xu, H. Chen, and S.-J. Zhang, “Charged superradiant instability of spherically symmetric regular black holes in de Sitter spacetime: time- and frequency-domain analysis,” *Eur. Phys. J. C* **86** (2026) 523, [arXiv:2602.00518](#).
- [36] D. R. Brill and J. A. Wheeler, “Interaction of neutrinos and gravitational fields,” *Rev. Mod. Phys.* **29** (1957) 465.
- [37] S. Chandrasekhar, *The Mathematical Theory of Black Holes*. Oxford University Press, 1983.
- [38] W. G. Unruh, “Absorption cross section of small black holes,” *Phys. Rev. D* **14** (1976) 3251.
- [39] B. R. Iyer and A. Kumar, “Note on the absence of massive fermion superradiance from a Kerr black hole,” *Phys. Rev. D* **18** (1978) 4799.
- [40] F. Finster, N. Kamran, J. Smoller, and S.-T. Yau, “Non-existence of time-periodic solutions of the Dirac equation in an axisymmetric black hole geometry,” *Commun. Math. Phys.* **205** (1999) 249, [arXiv:gr-qc/9905047](#).
- [41] D. Batic, M. Nowakowski, and K. Morgan, “The problem of embedded eigenvalues for the Dirac equation in the Schwarzschild black hole metric,” *Universe* **2** (2016) 31, [arXiv:1701.03889](#).

- [42] W. M. Jin, “Scattering of massive Dirac fields on the Schwarzschild black hole spacetime,” *Class. Quantum Grav.* **15** (1998) 3163–3175, [arXiv:gr-qc/0009009](#).
- [43] H. T. Cho, “Dirac quasinormal modes in Schwarzschild black hole space-times,” *Phys. Rev. D* **68** (2003) 024003, [arXiv:gr-qc/0303078](#).
- [44] S. R. Dolan and D. Dempsey, “Bound states of the Dirac equation on Kerr spacetime,” *Class. Quantum Grav.* **32** (2015) 184001, [arXiv:1504.03190](#).
- [45] Y. Huang, D.-J. Liu, X.-H. Zhai, and X.-Z. Li, “Massive charged Dirac fields around Reissner-Nordström black holes: quasibound states and long-lived modes,” *Phys. Rev. D* **96** (2017) 065002, [arXiv:1708.04761](#).
- [46] C. A. Sporea, “Quasibound states of the Dirac field in Schwarzschild and Reissner–Nordström black hole backgrounds,” *Mod. Phys. Lett. A* **34** (2019) 1950323, [arXiv:1905.05086](#).
- [47] R. A. Konoplya and A. Zhidenko, “Quasinormal modes of massive fermions in Kerr spacetime: long-lived modes and the fine structure,” *Phys. Rev. D* **97** (2018) 084034, [arXiv:1712.06667](#).
- [48] G.-S. Chen, C.-B. Yang, S.-S. Bao, Y. Tang, and Y.-L. Wu, “Revisiting the fermionic quasibound states around Schwarzschild black holes with improved analytic spectrum,” *Phys. Rev. D* **111** no. 12, (2025) 125006, [arXiv:2501.08881 \[gr-qc\]](#).
- [49] J. Li, H. Ma, and K. Lin, “Dirac quasinormal modes in spherically symmetric regular black holes,” *Phys. Rev. D* **88** (2013) 064001, [arXiv:1308.6499](#).
- [50] H. Ma and J. Li, “Dirac quasinormal modes of Born-Infeld black hole spacetimes,” *Chinese Phys. C* **44** (2020) 095102.
- [51] D. Batic and H. Schmid, “The Dirac propagator in the Kerr-Newman metric,” *Prog. Theor. Phys.* **116** (2006) 517, [arXiv:gr-qc/0606050](#).
- [52] I. M. Ternov, A. B. Gaina, and G. A. Chizhov, “Finite motion of electrons in the field of microscopic black holes,” *Sov. Phys. J.* **23** (1980) 695–700.
- [53] E. W. Leaver, “An analytic representation for the quasi-normal modes of Kerr black holes,” *Proc. R. Soc. A* **402** (1985) 285.
- [54] C. Gundlach, R. H. Price, and J. Pullin, “Late-time behavior of stellar collapse and explosions. I. Linearized perturbations,” *Phys. Rev. D* **49** (1994) 883–889, [arXiv:gr-qc/9307009](#).
- [55] Y. Hua and T. K. Sarkar, “Matrix pencil method for estimating parameters of exponentially damped/undamped sinusoids in noise,” *IEEE Trans. Acoust. Speech Signal Process.* **38** (1990) 814–824.
- [56] T. K. Sarkar and O. Pereira, “Using the matrix pencil method to estimate the parameters of a sum of complex exponentials,” *IEEE Antennas Propag. Mag.* **37** (1995) 48–55.
- [57] E. Berti, V. Cardoso, J. A. Gonzalez, and U. Sperhake, “Mining information from binary black hole mergers: a comparison of estimation methods for complex exponentials in noise,” *Phys. Rev. D* **75** (2007) 124017, [arXiv:gr-qc/0701086](#).
- [58] J. Jing, “Late-time evolution of charged massive Dirac fields in the Reissner-Nordström black-hole background,” *Phys. Rev. D* **72** (2005) 027501, [arXiv:gr-qc/0408090](#).